Perovskite Catalysts for Pure-Water-Fed Anion-Exchange-Membrane Electrolyzer Anodes: Co-Design of Electrically Conductive Nanoparticle Cores and Active Surfaces

Tingting Zhai[1,2,‡], Hao Wang[3,‡], Sarah R. Beaudoin[2], Ran Zhang[3], Minkyoung Kwak[2,4], Shujin Hou[4], Zhengxiao Guo[1,5*], Shannon W. Boettcher[2,4,6*]

[1]*Department of Mechanical Engineering, The University of Hong Kong, Hong Kong (SAR) 999077, China.*

[2]*Oregon Center for Electrochemistry, Department of Chemistry and Biochemistry, University of Oregon, Eugene, OR 97403, USA.*

[3]*Pingyuan Laboratory, and College of Chemistry, Zhengzhou University, Zhengzhou 450001, China.*

[4]*Department of Chemical & Biomolecular Engineering and Department of Chemistry, University of California, Berkeley, CA 94720, USA.*

[5]*Department of Chemistry, The University of Hong Kong, Hong Kong (SAR) 999077, China.*

[6]*Energy Storage and Distributed Resources Division, Lawrence Berkeley National Laboratory, Berkeley, CA 94720, USA.*

[*]Email: boettcher@berkeley.edu; zxguo@hku.hk

ABSTRACT

Anion-exchange-membrane water electrolyzers (AEMWEs) are a possible low-capital expense, efficient, and scalable hydrogen-production technology with inexpensive hardware, earth-abundant catalysts, and pure-water. However, pure-water-fed AEMWEs are still at an early stage of development and suffer from inferior performance compared to proton-exchange-membrane water electrolyzers (PEMWEs). One key challenge is to develop effective non-platinum group metal (non-PGM) anode catalysts and electrodes in pure-water-fed AEMWEs. We show how $LaNiO_3$-based perovskite oxides can be tuned by co-substitution on both A- and B-sites to simultaneously maintain high metallic electrical conductivity along with self-limiting surface reconstruction to expose stable Co-based active catalyst. The optimized perovskite, $Sr_{0.1}La_{0.9}Co_{0.5}Ni_{0.5}O_3$, yielded pure-water AEMWEs operating at 1.97 V at 2 A cm^{-2} at 70 °C with pure-water feed, thus illustrating the utility of the catalyst design principles.

INTRODUCTION

There are several relevant low-temperature electrolysis technologies[1,2] possibly suited to produce inexpensive H_2 taking advantage of variable renewable electricity production.[3-5] Alkaline water electrolyzers (AWEs) are well established and typically use ~30 wt. % KOH electrolyte that is at ~80 °C with the two electrodes being non-platinum-group metal (non-PGM) catalysts separated by a porous diaphragm. AWEs have historically suffered from limited current density (< 500 mA cm^{-2}) due to the higher internal resistance of the thick diaphragm and mass-transfer resistance from accumulated bubbles on the electrodes, although advanced systems are working to overcome these limitations.[6] Gas crossover through the porous separator further limits the ability to operate at differential pressure as well as the output H_2 purity.[7] To address these limitations, proton-exchange-membrane water electrolyzers (PEMWEs) were developed. Modern PEMWEs operate at high current density of 2–4 A cm^{-2} and differential pressure (200–400 psi) with a low degradation rate of < 20 μV h^{-1}.[8] However, the locally acidic and corrosive environment due to the acidic perfluorinated polymeric membrane requires expensive acid-resistant catalysts (IrO_2 and Pt), which does limit scalability.[2,9] Less-expensive components for the cell hardware and substantially reduced use of PGM catalysts are needed to achieve the cost and scale targets for H_2 production.

Combining advantages of AWEs and PEMWEs, the anion-exchange-membrane water electrolyzers (AEMWEs) enable a zero-gap configuration and differential pressure operation, with pure water or supporting-electrolyte feed.[10-12] AEMWEs may also be able to better tolerate less-pure water sources compared to PEMWEs, which could decrease system complexity, operational costs, and robustness.[13] The alkaline environment permits the use of inexpensive hardware components and earth-abundant catalysts.[14] However, current pure-water-fed AEMWEs yield far lower performance as PEMWEs in terms of efficiency (~ 65 kWh/kg_{H2}) and durability (typically >1 mV h^{-1} performance loss in the AEMWE).[15] To compensate for the drawbacks of membranes/ionomers and anode catalysts, supporting electrolytes, such as aq. KOH or K_2CO_3, are commonly fed to AEMWEs to reduce the ionic resistance of membrane and catalyst layer and increase durability. An example AEMWE fed with 1.0 M KOH electrolyte has demonstrated ~ 2 A

cm^{-2} at ~ 1.8 V, which approaches the performance of PEMWEs.[16] The use of corrosive alkaline electrolytes, however, is a drawback to the membrane electrolyzer system, which can lead to shunt currents and hardware corrosion issues at the system level. The ultimate target for AEMWEs is to realize comparable performance of PEMWEs with the electrolyte-free (nominally pure water) feed but non-PGM catalysts and non-fluorocarbon membranes.

One challenge for AEMWE technology is the difficulty in designing non-noble-metal OER catalysts specifically for pure-water-fed AEMWEs with nearly all OER-catalyst development having been done in liquid alkali environments.[17] Still, the most common anode catalysts for AEMWEs are Ir-based catalysts as they are electrically conductive, largely insoluble under OER conditions, and have modest OER activity in basic media.[18,19] In liquid-electrolyte-fed AEMWEs, Ni-Fe (oxy)hydroxide, and related, catalysts show excellent OER activity, as they do in liquid-alkaline media. These oxyhydroxides, however, tend to have poor performance and durability in pure-water-fed AEMWEs, probably due to the lower electrical conductivity of hydroxides (10^{-5} mS cm^{-1}), which fail to fully oxidize to more-conductive oxyhydroxides without liquid electrolyte, along with the possible dissolution and loss of soluble Fe species.[17,20,21] Metal-oxide nanoparticles with higher electrical conductivity have tended to exhibit better performance. For example, Co_3O_4 (~ 0.2 mS cm^{-1}) anode catalysts had nearly the performance to IrO_2 despite having the electrical conductivity (all reported conductivities are measured for the samples here, see below) almost a million times lower than that of the IrO_2 ($1.4 \pm 0.1 \times 10^5$ mS cm^{-1}).[18] The conductivity of Co_3O_4, however, remains far from optimal.

While most non-noble-metal oxides are electrical insulators or semiconductors, some classes of perovskite oxides exhibit high metallic conductivities.[22,23] $LaNiO_3$, in the family of ABO_3 perovskites, exhibits metallic behaviour with electrical conductivity of $4.3 \pm 0.1 \times 10^5$ mS cm^{-1}.[24] However, $LaNiO_3$ alone is a very poor catalyst for the OER in alkaline conditions and is only activated for OER by absorption of Fe-impurities and through the formation of NiFeOOH surface species.[25] The catalytic, electrochemical, and electrical properties of $LaNiO_3$ can be, however, systematically controlled by cation substitution at

both A and B sites. One underlying challenge is the high-temperature synthesis of $LaNiO_3$ (usually > 700 °C), leading to the large particle size and low density of active sites.

In this work, we leverage the high electrical conductivity of crystalline $LaNiO_3$ and illustrate how strategic cation substitution can be used to simultaneously control and optimize over the *i*) electrical conductivity, *ii*) surface reconstruction, and *iii*) active-surface-phase composition. We show that the electrical conductivity and degree of reconstruction can be controlled and tuned by substitution of Co onto the Ni sites in $LaNiO_3$. While the pure $LaCoO_3$ compound is a semiconductor with low electrical conductivity, the $LaCo_xNi_{1-x}O_3$ series shows orders of magnitude higher electrical conductivities ($2.3 \pm 0.1 \times 10^5$ mS cm^{-1} to $1.1 \pm 0.1 \times 10^5$ mS cm^{-1}) for a broad range of x values from 0.3 up to 0.7. The addition of Co also suppresses the degree of surface structure reconstruction, leading to more morphologically stable catalyst nanoparticles.

We found that A-site substitution of La with Sr reduced the particle sizes, roughly doubling the BET surface area. Sr, being also much more soluble as $Sr(OH)_2$ than La as $La(OH)_3$ in basic media, enables further tuning of the degree of surface amorphization. Thus, through systematic understanding and design, we report $Sr_{0.1}La_{0.9}Co_{0.5}Ni_{0.5}O_3$ anode catalyst powders which have the state-of-the-art performance in pure-water-fed AEMWEs at 70 °C, achieving cell voltage of 1.81 V at 1 A cm^{-2} and 1.97 V at 2 A cm^{-2}. These results are among the best reported for pure-water-fed AEMWEs, closing in on those of the alkaline-electrolyte-fed AEMWE (~ 1.8 V at ~ 2 A cm^{-2}),[19,26-28] although still somewhat higher than established PEMWE technologies with PGM catalysts (~ 1.7 V at ~ 2 A cm^{-2}).[29-31] This work thus establishes key design rules for crystalline metallic-conductive non-precious metal-oxide OER catalysts where the electrical conductivity, surface reactivity/restructuring, and catalytic surface composition are together co-designed through systematic manipulation of the solid-state chemistry.

RESULTS AND DISCUSSION

Structure characterization, electrical conductivity and morphology of perovskites. The $Sr_yLa_{1-y}Co_xNi_{1-x}O_3$ series (x = 0, 0.3, 0.5, 0.7, 1; y = 0, 0.1, 0.2, 0.3) were synthesized

via a citric-acid sol-gel method from nitrate salts followed by decomposition of the organic species and nitrates at 700 ℃ in air. The crystalline structures of Sr-doped $LaCo_xNi_{1-x}O_3$ (x = 0, 0.3, 0.5, 0.7, 1) were investigated by powder X-ray diffraction (XRD) analysis (**Figures 1a**, **S1–S3** and **Table S1**). The results show that all synthesized powders adopt a rhombohedral perovskite structure (space group: R-3m), comprising eight tilted corner-sharing BO_6 octahedra (where B = Ni, Co) with a central cavity accommodating La^{3+}/Sr^{2+} ions.[32] Rietveld refinement of the representative $Sr_{0.1}La_{0.9}Co_{0.5}Ni_{0.5}O_3$ sample (**Figure 1a**) confirms this structure, yielding lattice parameters a = 5.46 Å and c = 13.17 Å with low residuals (R_{wp} = 6.73%, R_p = 7.98%, Table S1). Full XRD patterns for all samples (**Figures S1–S5**) exhibit consistent rhombohedral symmetry, with minor peak shifts attributed to ionic radius differences between dopants. No impurities were detected in any of the as-prepared samples. For the $LaCo_xNi_{1-x}O_3$ series (**Figure S2**), the characteristic diffraction peaks (e.g., strongest peak near $2\theta = 33^{\circ}$) shifted incrementally towards higher angles with increasing Co^{3+}/Ni^{3+} ratios. This shift is attributed to the smaller ionic radius of Co^{3+} (0.54 Å) relative to Ni^{3+} (0.56 Å). In contrast, when Sr^{2+} is introduced into the $Sr_yLa_{1-y}Co_{0.5}Ni_{0.5}O_3$ structure (y = 0.1, 0.2, 0.3), the lattice constant increases relative to $LaCo_{0.5}Ni_{0.5}O_3$ (**Figure S3**), due to the larger ionic radius of Sr^{2+} (1.18 Å) compared to La^{3+} (1.03 Å). XRD patterns of Fe-doped $Sr_yLa_{1-y}Co_{0.5}Ni_{0.5}O_3$ also show no detectable impurity phases (**Figures S4–S5**).

The electrical conductivities of $LaCo_xNi_{1-x}O_3$ (x = 0, 0.3, 0.5, 0.7, 1) and Sr/Fe doped $LaCo_xNi_{1-x}O_3$ perovskites were measured at room temperature using a four-probe method (**Figure 1b**). The through-plane conductivity of commercial Co_3O_4 (30–50 nm) powder was determined by two electrode polarization curves due to its high electrical resistance.[20] $LaNiO_3$ exhibited a high electrical conductivity of $4.3 \pm 0.1 \times 10^5$ mS cm^{-1}, consistent with the metallic behavior,[22] and significantly higher than that of $LaCoO_3$ ($1.2 \pm 0.2 \times 10^2$ mS cm^{-1}) and commercial Co_3O_4 (30–50 nm, $2.0 \pm 0.8 \times 10^{-1}$ mS cm^{-1}) as in Figure 1b. Although Co substitution at the Ni site in $LaNiO_3$ reduces the electrical conductivity, $LaCo_{0.5}Ni_{0.5}O_3$ retains a high electrical conductivity of $1.9 \pm 0.1 \times 10^5$ mS cm^{-1}. Sr doping to yield $Sr_{0.1}La_{0.9}Co_{0.5}Ni_{0.5}O_3$ leads to a small decrease in electrical conductivity ($1.6 \pm 0.1 \times 10^5$ mS cm^{-1}), but is still comparable to commercial IrO_2 ($1.4 \pm 0.1 \times 10^5$ mS cm^{-1}).

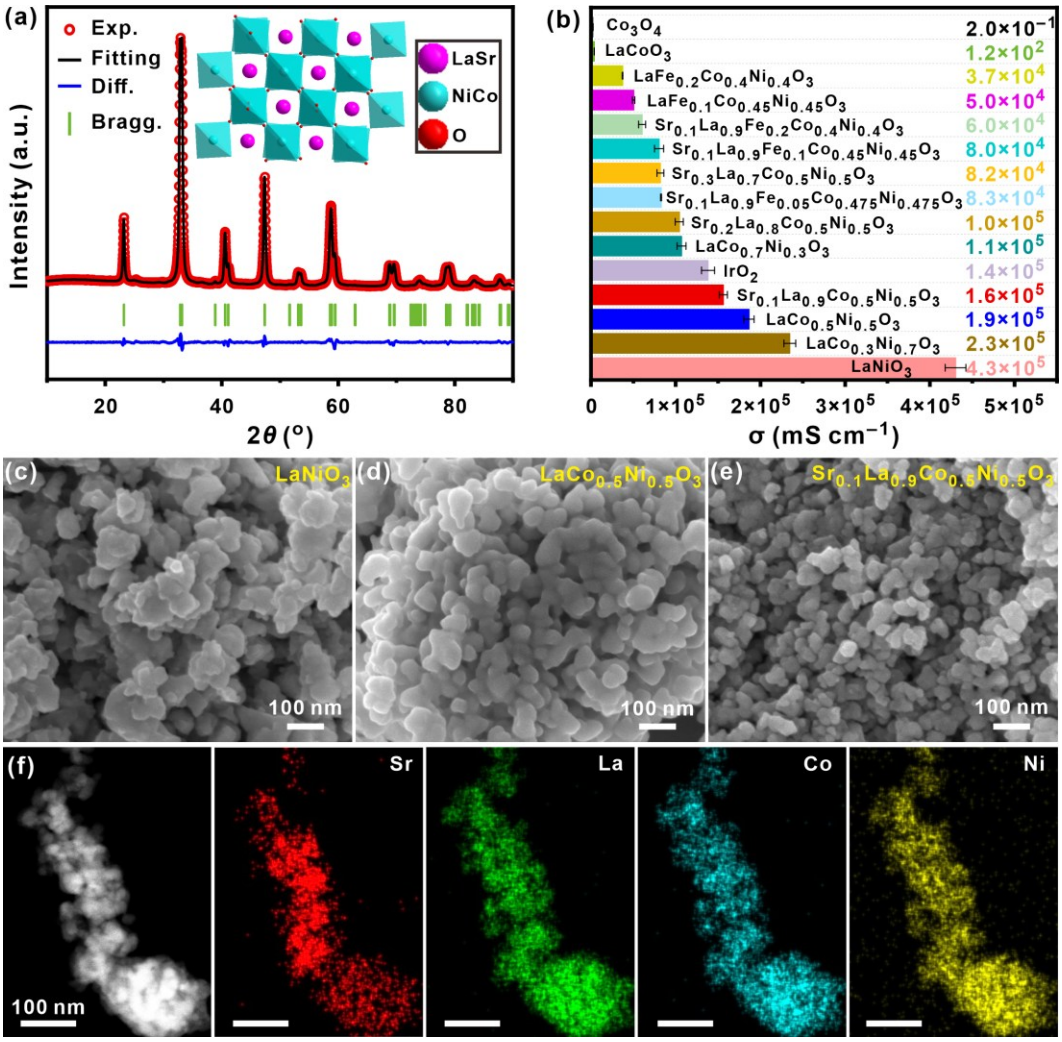

Figure 1. Crystal structure, electrical conductivity and morphology of the prepared perovskite oxide catalysts. (a) Observed and calculated XRD pattern and their difference of $Sr_{0.1}La_{0.9}Co_{0.5}Ni_{0.5}O_3$, the inset is its schematic representation of the crystal structure. (b) Electrical conductivities of all synthesized perovskites, commercial Co_3O_4 and IrO_2 at room temperature. SEM images of (c) $LaNiO_3$, (d) $LaCo_{0.5}Ni_{0.5}O_3$ and (e) $Sr_{0.1}La_{0.9}Co_{0.5}Ni_{0.5}O_3$. (f) HAADF-STEM image and corresponding EDS elemental mapping of $Sr_{0.1}La_{0.9}Co_{0.5}Ni_{0.5}O_3$.

The morphologies and microstructures of the as-prepared samples were characterized using scanning electron microscopy (SEM) and transmission electron microscopy (TEM) (**Figures 1c–f** and **S6–S9**). $LaNiO_3$ and $LaCoO_3$ had sizes of 98 ± 26 nm and 109 ± 35 nm, respectively, with the distribution of sizes spanning 50 to 200 nm. $LaCo_{0.5}Ni_{0.5}O_3$ had

more-uniform distribution and smaller particle size, 78 nm ± 20 nm. Substitution with Sr led to a decrease in particle size, with $Sr_{0.1}La_{0.9}Co_{0.5}Ni_{0.5}O_3$ at 56 nm ± 11 nm (**Figures S6–S9**). The Brunauer-Emmett-Teller (BET) specific surface area of the perovskites, commercial Co_3O_4, and IrO_2 were fitted by N_2 adsorption-desorption isotherms (**Table S2**). $LaCo_{0.5}Ni_{0.5}O_3$ (8.9 ± 0.2 m^2 g^{-1}) and $Sr_{0.1}La_{0.9}Co_{0.5}Ni_{0.5}O_3$ (13.6 ± 0.1 m^2 g^{-1}) exhibited higher surface area than $LaNiO_3$ (8.8 ± 0.2 m^2 g^{-1}) and $LaCoO_3$ (7.7 ± 0.1 m^2 g^{-1}), consistent with the SEM observations. High-angle annular dark-field STEM (HAADF−STEM) images and corresponding energy-dispersive X-ray spectroscopy (EDS) elemental mapping showed uniform distribution of all elements (**Figure 1f**). The stoichiometric ratio of metal elements in key samples were verified by inductively coupled plasma-mass spectroscopy (ICP-MS) (**Table S3**) and were consistent with the intended synthesis ratios.

Electrocatalytic performance and relation to materials and interface properties. The electrocatalytic performance and durability of the as-prepared perovskites, commercial Co_3O_4 and IrO_2 were evaluated in AEMWEs at 70 ºC with electrolyte-free water feed (see details in supporting information). Catalyst powder and ionomer were dispersed in isopropyl alcohol and water and sprayed on porous-transport layers (PTLs) with the catalyst mass loading of 3.0 ± 0.2 mg cm^{-2}. The membrane-electrode assemblies (MEAs) were constructed using various anode catalysts on stainless-steel woven mesh, a 40 μm TP-85 membrane and a Pt black cathode catalyst on Toray-090 carbon paper with a high mass loading of 3.0 ± 0.2 mg cm^{-2}. Pt black was selected for its high HER activity, reproducibility, and stability under pure-water operation, compared to commercial Pt/C (40 wt%) (**Figure S10**), which is critical for our studies focused on the anode. The above components were compressed together under 55 in-lb by applying a torque wrench to ensure uniform contact of the assembly. MEA configurations remained consistent across all AEMWE measurements, with only the anode catalyst varying between samples.

The current-voltage polarization curves for different catalysts were recorded over a current range of 10–2000 mA cm^{-2} (without *iR*-compensation) to assess their catalytic activities in AEMWEs (**Figure 2a**). All perovskite oxides had higher performance than commercial

Co_3O_4 and IrO_2. The cell voltage measured at low current is related to the catalytic activity of the anode, as ohmic and mass-transport loss are negligible in this region.[10,18] At 10 mA cm^{-2}, the cell voltages for perovskite oxides were 100–150 mV lower than that of commercial Co_3O_4. The voltage difference between the cells with the perovskite oxides and the commercial Co_3O_4 widens as the current density increases, likely due to the reduced voltage drop in the porous electrode due to the superior electrical conductivities of perovskite oxides.

Among the tested perovskites, $Sr_{0.1}La_{0.9}Ni_{0.5}Co_{0.5}O_3$ yielded the best cell performance with 1.81 and 1.97 V at current densities of 1 and 2 A cm^{-2}, respectively, outperforming commercial Co_3O_4 (2.13 V at 1 A cm^{-2} and 2.36 V at 2 A cm^{-2}) and IrO_2 (1.99 V at 1 A cm^{-2} and 2.19 V at 2 A cm^{-2}). $Sr_{0.1}La_{0.9}Ni_{0.5}Co_{0.5}O_3$ also exhibited the smallest potential at the small current of 0.025 mA cm^{-2}_{BET}, highlighting its superior intrinsic OER activity (see BET-normalized currents in **Figure S11**). $LaNi_{0.5}Co_{0.5}O_3$ also exhibited good performance (2.07 V at 2 A cm^{-2}), relative to pristine perovskite oxides, $LaNiO_3$ (2.12 V at 2 A cm^{-2}) and $LaCoO_3$ (2.10 V at 2 A cm^{-2}). The AEMWE performance of $LaCo_xNi_{1-x}O_3$ (x = 0, 0.3, 0.5, 0.7 and 1), $Sr_yLa_{1-y}Co_{0.5}Ni_{0.5}O_3$ (y = 0, 0.1 and 0.2), $LaFe_zCo_{0.5-z/2}Ni_{0.5-z/2}O_3$ (z = 0, 0.1 and 0.2) and $Sr_{0.1}La_{0.9}Fe_zCo_{0.5-z/2}Ni_{0.5-z/2}O_3$ (z = 0, 0.05, 0.1 and 0.2) are compared in **Figures S12–S15**.

To deconvolute the cell equivalent resistances, galvanostatic electrochemical impedance spectroscopy (GEIS) was conducted at 50 mA cm^{-2}. The mass-transfer resistance was assumed to be negligible at this low current density. The Nyquist plots and fitted results are shown in **Figure 2b–c**, with the equivalent circuit model. The equivalent circuit includes an ohmic resistance R_{ohm} in the high-frequency region and two additional circuits in low-frequency region (each comprising a resistor and constant phase element in parallel — $R_{ct,1}$, $R_{ct,2}$ with CPE1 and CPE2). The total charge-transfer resistance is determined using the equation: $R_{ct} = R_{ct,1} + R_{ct,2}$. R_{ohm} reflects the total ionic resistance of membrane, and the electrical resistance at all MEA contact interfaces and is largely independent of the applied voltage.

All tested perovskite oxides exhibited similar R_{ohm} (0.10–0.12 Ω cm^2), slightly lower than that of commercial Co_3O_4 (0.143 ± 0.015 Ω cm^2), likely attributed to better electrical contact from the higher-conductivity perovskite catalysts. $LaNiO_3$ and IrO_2 demonstrated the lowest ohmic resistance (0.101 ± 0.003 Ω cm^2 and 0.096 ± 0.003 Ω cm^2), also consistent with their high electrical conductivity (measured to be 4.3 ± 0.1 × 10^5 mS cm^{-1} and 1.4 ± 0.1 × 10^5 mS cm^{-1}, respectively, using the methods described herein). $LaCoO_3$ exhibited a higher ohmic resistance (0.124 ± 0.006 Ω cm^2), probably due to its lower electrical conductivity (here measured to be 1.2 ± 0.2 × 10^2 mS cm^{-1}) relative to the other perovskites. Even with 10% Sr and 50% Co substitution at La site and Ni site of $LaNiO_3$, respectively, $Sr_{0.1}La_{0.9}Co_{0.5}Ni_{0.5}O_3$ maintained a low ohmic resistance of 0.11 ± 0.01 Ω cm^2.

At 2 A cm^{-2}, the difference between the catalysts with the lowest R_{ohm} of ~0.10 Ω cm^2 and those with the highest of ~0.14 Ω cm^2 would lead to a cell voltage difference of ~80 mV. The difference in cell performance, however, between the best conductive perovskite catalysts and the baseline Co_3O_4 at 2 A cm^{-2} is ~400 mV. This can be explained by the observed trend in apparent R_{ct}. The electrode kinetics are a function of potential. To assess the relative effect of kinetics, we plot $R_{ct} = R_{ct,1} + R_{ct,2}$ from the impedance analysis at 50 mA cm^{-2} where kinetic resistances are expected to be substantial. $Sr_{0.1}La_{0.9}Co_{0.5}Ni_{0.5}O_3$ exhibited a R_{ct} of 1.03 ± 0.02 Ω cm^2, lower than that of baseline Co_3O_4 (1.46 ± 0.06 Ω cm^2). This lower apparently R_{ct} is likely due to a combination of faster OER kinetics from the active surfaces, and higher electrical conductivity which improves the electrical transport within the ionomer-filled porous electrode structure and thus effective surface area. The value of R_{ct} generally tracked the measured total cell voltage (**Figure 2c**).

The polarization curves for the different anode catalysts were then decomposed into *i*) the thermodynamic potential for water electrolysis (1.19 V at 70 °C), *ii*) the ohmic overpotential $\eta_{ohm} = iR_{ohm}$ where R_{ohm} taken from the high-frequency impedance in the fit above, *iii*) the kinetic overpotential (η_{kin}), which includes overall contributions from both the oxygen evolution reaction (OER) at the anode and the hydrogen evolution reaction (HER) at the cathode, calculated using the Tafel model from ohmic-loss-free cell voltages at current densities below 100 mA cm^{-2} (and extrapolated to all currents), and *iv*) the

residual overpotential (η_{res}) that is unexplained by *i*) - *iii*), which will be discussed below (**Figure 2d–e**).[33,34]

This analysis shows that η_{kin} is the predominant voltage loss across all catalysts. $Sr_{0.1}La_{0.9}Ni_{0.5}Co_{0.5}O_3$ achieved an η_{kin} as low as 0.48 V at 2 A cm^{-2}, which is 250 mV and 110 mV lower than that of the commercial Co_3O_4 (0.73 V) and commercial IrO_2 (0.59 V) (**Figure 2e**), respectively. This analysis is thus consistent with the lower R_{ct} from GEIS results. The calculated η_{ohm} increases with current density, representing 20–30% of the total cell voltage loss for these devices at 2 A cm^{-2}. Both $LaNiO_3$-based perovskites and commercial IrO_2 catalysts had 60–80 mV lower η_{ohm} at 2 A cm^{-2} than Co_3O_4, likely due to lower electrical resistance at the catalyst-PTL interface. We note that the PiperION membrane has a hydroxide ion conductivity of 0.1–0.2 S cm^{-1} at 70 °C leading to an expected contribution solely from the 40-μm membrane only 0.02–0.04 Ω.

We also note that the large variations in electrical conductivity across catalysts did not produce equally significant differences in η_{ohm}. This is because the electrical resistivity of the catalyst layer is not measured by the high frequency impedance that is used to find R_{ohm};[35] the porous electrode has parallel ionic and electrical conduction pathways resulting in the catalyst layer's ionic and electrical resistances being lumped into the equivalent impedance of associated with $R_{ct,1}$, $R_{ct,2}$, CPE1, and CPE2.

At lower current density (e.g., 100 mA cm^{-2}), residual overpotentials (η_{res}) were negligible across all catalysts (<1%). However, as the current density increased from 100 mA cm^{-2} to 2 A cm^{-2}, the η_{res} contribution increased to 10–20% of the total voltage loss. These observations suggest that a least a portion of η_{res} can be ascribed to mass-transfer-related losses, perhaps in combination with increasing overpotentials due to ion and electron transport through the resistive porous electrode's catalyst layer.

The double-layer capacitance (C_{dl}), estimated from the non-faradaic charging measured between 0.6 V to 1.0 V in the two-electrode electrolyzer configuration, was used to calculate the electrochemically active surface area (ECSA) for the catalysts (**Figure 2f**).[36]

In this two-electrode configuration the measured capacitance is determined by the smaller of the anode or cathode. Because of the large loading of Pt on porous carbon at the cathode, we expect measured capacitances to by roughly equal to that of the anode (i.e. $C_{tot} = C_{anode}$ $C_{cathode}/(C_{anode} + C_{cathode}) \approx C_{anode}$, when $C_{anode} << C_{cathode}$). This assumption was further confirmed that the C_{dl} of Pt black in a three-electrode system (0.1 M Fe-free KOH) was 65 times larger than that of $Sr_{0.1}La_{0.9}Co_{0.5}Ni_{0.5}O_3$ (**Figure S16**). The cell capacitances for $LaNiO_3$, $LaCoO_3$ and $LaCo_{0.5}Ni_{0.5}O_3$ systems were 5.0, 4.0 and 5.5 mF cm^{-2}, respectively, all lower than that of commercial Co_3O_4 (7.2 mF cm^{-2}) (**Figure S17**). This difference is in part attributed to the larger particle size for the perovskites after high-temperature annealing (700 °C). However, $Sr_{0.1}La_{0.9}Ni_{0.5}Co_{0.5}O_3$ and IrO_2 possess high C_{dl} of 27.3 and 11.2 mF cm^{-2}, respectively, although they have *smaller* BET surface areas of 13.6 ± 0.1 and 6.3 ± 0.1 m^2 g^{-1}, respectively, compared to commercial Co_3O_4 (91.3 ± 0.2 m^2 g^{-1}). $Sr_{0.1}La_{0.9}Ni_{0.5}Co_{0.5}O_3$ and IrO_2 therefore have more available surface redox-active species per unit BET surface area providing pseudocapacitive charging response.

The C_{dl} per gram was divided by BET surface area (area per gram) was used quantify the average surface redox/capacitance per internal microscopic surface area of catalyst (mF cm^{-2}_{micro}). All metallic catalysts, including $LaNiO_3$-based perovskites and IrO_2, had higher C_{dl}/BET than non-metallic Co_3O_4 (**Figure 2g**). The Co_3O_4 had the smallest C_{dl}/BET of 0.0026 mF cm^{-2}_{micro}, consistent with the low electrical conductivity (2.0 ± 0.8 mS cm^{-1}), meaning that only small portion of the Co_3O_4 near the metal current collector is likely electrochemically active, especially under high-current conditions for ohmic drops through electrode would lead to significant current heterogeneity. $LaNiO_3$, $LaCoO_3$ and $LaNi_{0.5}Co_{0.5}O_3$ had much higher C_{dl}/BET of 0.017-0.021 mF cm^{-2}_{micro}, compared to Co_3O_4, ascribed to the enhanced electrical conductivity. Notably, $Sr_{0.1}La_{0.9}Ni_{0.5}Co_{0.5}O_3$ had C_{dl}/BET of 0.067 mF cm^{-2}_{micro}, 25 times higher than Co_3O_4, and four times higher than metallic $LaNiO_3$. Sr leaching during electrolysis likely facilitates surface restructuring to form a thin layer of electrolyte-permeated oxyhydroxide phase with higher apparent capacitance per internal area due to Ni/Co redox.

Electrocatalytic durability of perovskite anodes in AEMWEs with pure-water feed.

The anode in the AEMWEs undergoes more- severe degradation than the cathode.[17,37] Previous studies have identified ionomer within the ionomer-catalyst porous anode structure as the primary factor limiting durability when pure water is used.[38] To understand how conductivity influences stability in pure-water-fed AEMWEs, we conducted 20-h durability tests at 70 °C under pure-water-fed conditions at 500 mA cm^{-2} using as-prepared perovskite oxides, IrO_2 and Co_3O_4 as anodes, a duration capturing substantial degradation (2.7–13.4 mV h^{-1}) across all samples due to rapid ionomer degradation (**Figures S18-S20**). The cell voltage with $Sr_{0.1}La_{0.9}Ni_{0.5}Co_{0.5}O_3$ increased from 1.71 V to 1.83 V over 20 h (a degradation rate of 5.0 mV h^{-1}, see also **Figure S19** for polarization curves before and after testing). The degradation rate of $Sr_{0.1}La_{0.9}Ni_{0.5}Co_{0.5}O_3$ is comparable to that of IrO_2 (5.1 mV h^{-1}), but inferior to commercial Co_3O_4 (2.7 mV h^{-1}). The faster degradation observed for $Sr_{0.1}La_{0.9}Ni_{0.5}Co_{0.5}O_3$ and IrO_2 compared to that of commercial Co_3O_4, is consistent with the higher electrical conductivity, which would accelerate ionomer degradation throughout the entire conductive-catalyst porous electrode[18] compared to commercial Co_3O_4 where the oxidation is limited to the interfacial region near the current collector. We note, however, the lack of anode catalyst's electrical conductivity is not a useful mechanism to stabilize AEMWE ionomer because of the performance loss – metallic catalysts are essential for achieving high active catalyst loading and hence the best cell performance. Indeed, $Sr_{0.1}La_{0.9}Ni_{0.5}Co_{0.5}O_3$ maintained a lower cell voltage than commercial Co_3O_4 after the 20-h test, despite a higher degradation rate. $LaNiO_3$-based devices degraded the fastest (13.4 mV h^{-1} over 20 h), likely due to combination of high electrical conductivity and poor catalytic activity compared to $Sr_{0.1}La_{0.9}Ni_{0.5}Co_{0.5}O_3$ leading to higher initial voltages (**Figure S20**). To further substantiate the critical role of ionomer degradation in stability loss, we highlight that introducing an HfO_x protective layer via atomic-layer deposition following our prior report[39] significantly enhanced stability in pure-water AEMWE configurations (**Figure 2h**). This direct correlation between ionomer preservation and operational durability offers one pathway to decouple stability from conductivity constraints, but requires more development.

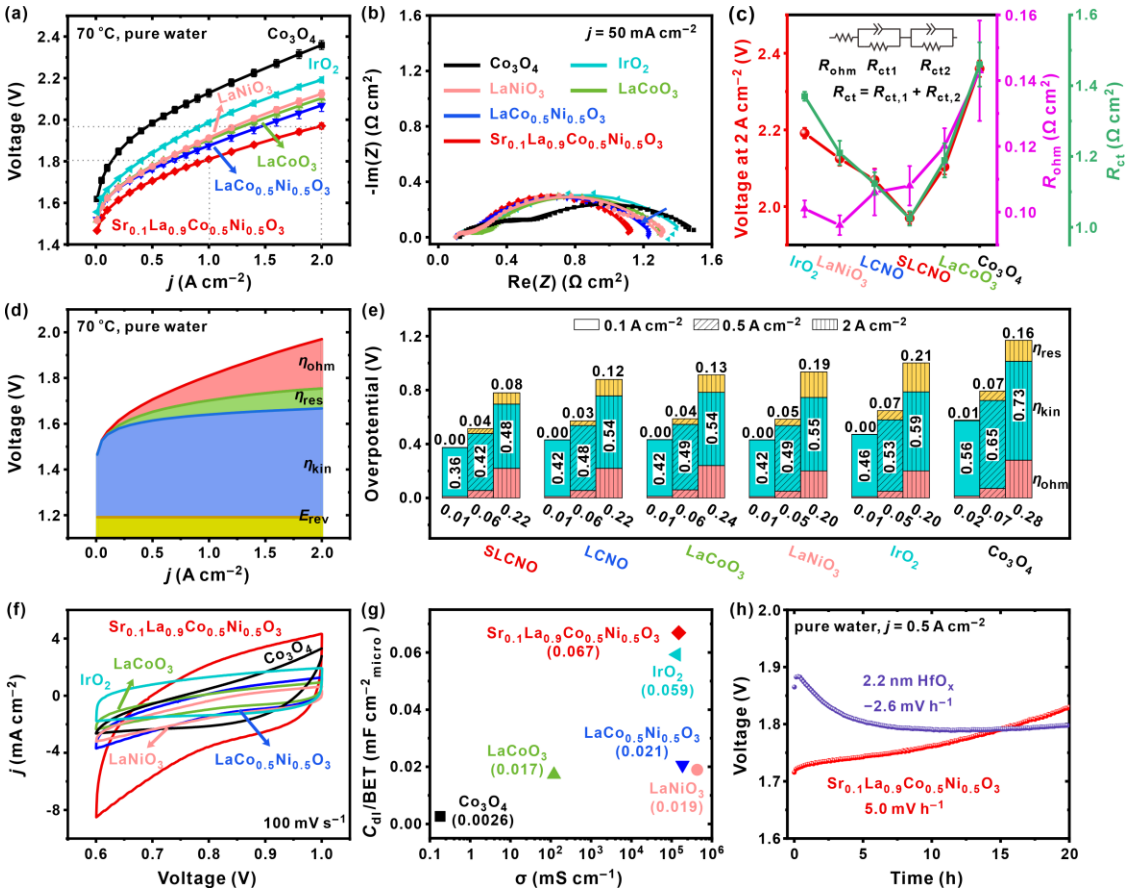

Figure 2. Electrochemical performance of as-prepared catalysts and commercial Co_3O_4 (30–50 nm). (a) Polarization curves of AEMWEs with different anode catalysts in pure water at 70 °C, with current density normalized by the geometric area of the anode. The indicated catalysts/10 wt% PiperION ionomer on stainless-steel woven substrate, TP-85 membrane, and Pt black/10 wt% PiperION ionomer on Toray carbon paper were used as the anode, membrane, and cathode, respectively (data presented as mean ± one standard deviation). (b) Nyquist plots of total cell impedance at 50 mA cm^{-2} for different anode catalysts tested in pure-water AEMWE. The data is fitted by the inset equivalent circuit. (c) AEMWE cell voltage at 2 A cm^{-2}, the ohmic resistance (R_{ohm}) and charge-transfer resistance (R_{ct}) with different anode catalysts. Reported data is the average fitting results of three Nyquist plots for each sample. (d) Cell voltage distribution for $Sr_{0.1}La_{0.9}Co_{0.5}Ni_{0.5}O_3$ sample. (e) Potential loss at 0.1 A cm^{-2}, 0.5 A cm^{-2} and 2.0 A cm^{-2}. (η_{ohm}: ohmic overpotential, η_{kin}: kinetic overpotential and η_{res}: residual overpotential). (f) Cyclic voltammetry (CV) curves of the AEMWE device in a non-faradaic region with different anode catalysts at a scan rate of 100 mV s^{-1}. (g) Electrochemical double-layer capacitance per BET surface area (C_{dl}/BET) of AEMWE with different anode catalysts. Average of anodic and cathodic current densities at 0.8 V as a function of the scan rate. (h) Durability tests for $Sr_{0.1}La_{0.9}Co_{0.5}Ni_{0.5}O_3$ and 2.2 nm HfO_x-coated $Sr_{0.1}La_{0.9}Co_{0.5}Ni_{0.5}O_3$ anode catalysts held at 0.5 A cm^{-2} for 20 h at 70 °C in AEMWE with pure water feed. SLCNO and LCNO in Figure 2(c) and (e) are $Sr_{0.1}La_{0.9}Co_{0.5}Ni_{0.5}O_3$ and $LaCo_{0.5}Ni_{0.5}O_3$, respectively.

Postmortem analysis of the ionomer degradation and catalyst reconstruction. To investigate the degradation mechanism(s), the AEMWE cell was disassembled for

postmortem analysis. After operation, the anode was soaked in 3 M aq. NaCl to exchange OH^- with Cl^- and prevent further degradation from OH^- nucleophilic attack upon drying. Surface and cross-sectional SEM analysis were performed on $Sr_{0.1}La_{0.9}Co_{0.5}Ni_{0.5}O_3$ to reveal morphological and microstructural changes (**Figure 3b–c** and **3e–f**). After the stability test, significant ionomer degradation was observed on the surface of the catalyst layer (**Figure 3c**). This near-complete ionomer degradation within the catalyst layer was further substantiated by EDS mapping analysis (**Figure S21**), which demonstrated a significant reduction in C and N content (elemental markers of the ionomer) after operation. Cross-sectional SEM images revealed only perovskite nanoparticles comprising the post-mortem porous electrode, with higher-magnification views (**Figure 3e–f**) showing a discernible absence of ionomer in the catalyst layer after 20-h operation. These findings indicate almost-complete ionomer degradation within the catalyst layer during operation and are consistent with the high electrical conductivity leading to uniform oxidizing potential and fast degradation throughout the catalyst/ionomer anode layer. In stark contrast, surface SEM-EDS mapping and cross-sectional SEM imaging analysis of post-mortem Co_3O_4 anodes reveals retained ionomer on the catalyst layer's top surface, but severe cracking and delamination of catalyst particles and ionomer from the PTL (**Figures S22-S23**). This localized failure stems from aggressive ionomer oxidation at the PTL interface, which disrupts catalyst adhesion and leads to catastrophic mechanical degradation.

X-ray photoelectron spectra of PiperION ionomer before and after testing with $Sr_{0.1}La_{0.9}Co_{0.5}Ni_{0.5}O_3$ catalyst also show the chemical signature of degradation (**Figure S24**). In the C 1s spectra, a new high-binding-energy C–O peak and a reduced-intensity C–N peak was observed, indicating oxidation of the phenyl group and a loss of C–N content in the ionomer after operation. For the N 1s and F 1s spectra, a new N 1s peak emerged around 400 eV, and the intensities of both the nitrogen cation peak and the fluorine peak decreased post-operation, further confirming anode-ionomer decomposition during the electrochemical tests.[38,39] Moreover, ^{1}H NMR and ATR-FTIR were conducted to further analyze the ionomer (PiperION) pre- and post-operation. The ^{1}H NMR spectrum post-test reveals new signals at 4.8, 5.3, and 6.5 ppm (**Figure S25**), suggesting the Hofmann ring-opening elimination, which is due to hydroxide nucleophilic attack.[40,41] In addition, a

reduction in the intensity of the methyl proton peak attached to the quaternary ammonium group at 3.1 ppm further supports the degradation of the quaternary ammonium charged groups. ATR-FTIR shows evidence of oxidation: the pristine C=C stretching band at 1616 cm^{-1} transforms into multiple peaks in the region of 1667 – 1540 cm^{-1}, likely due to the formation of new C=C or C=O bonds resulting from phenyl oxidation.[42] Furthermore, the C-N stretching vibration (1221 cm^{-1}) weakens and shifts, while a new C-O bond signal emerges at 1079 cm^{-1} (**Figure S26**).[43] These results support ionomer prominent degradation modes via C-N bond cleavage and phenyl oxidation. Developing oxidation-resistant ionomers or optimizing the conductive catalyst-ionomer interface remains important for improving AEMWE stability.[39]

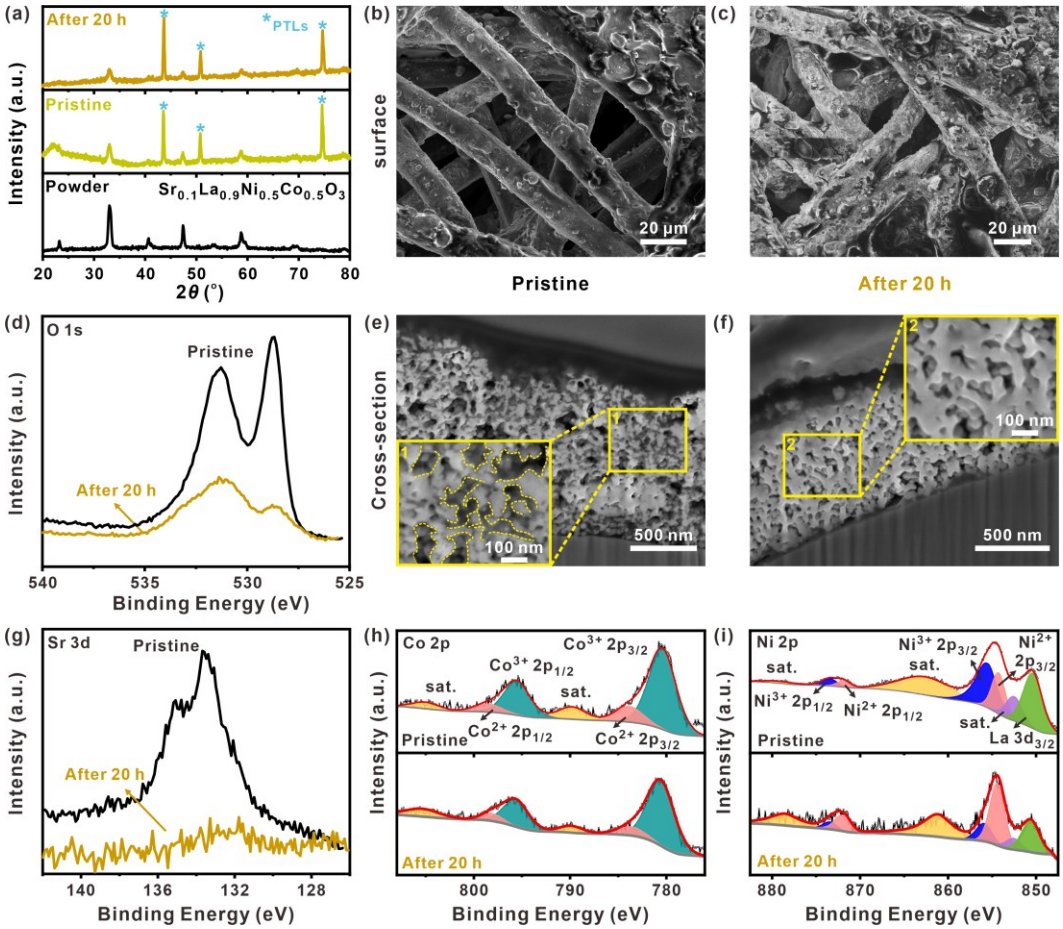

Figure 3. Structure and oxidation state of $Sr_{0.1}La_{0.9}Co_{0.5}Ni_{0.5}O_3$ on PTLs before and after operation. (a) XRD patterns of $Sr_{0.1}La_{0.9}Co_{0.5}Ni_{0.5}O_3$ on porous transport layers (PTLs) before and after 20 h stability test at 0.5 A cm^{-2}. Surface SEM images of (b) pristine and (c) after 20 h stability test of $Sr_{0.1}La_{0.9}Co_{0.5}Ni_{0.5}O_3$ sample on PTLs. Cross-sectional SEM images of (e) pristine and (f) after 20 h stability test of $Sr_{0.1}La_{0.9}Co_{0.5}Ni_{0.5}O_3$ sample on PTLs (The ionomer appears as the dark

region outlined by yellow dashed lines (region 1), while the catalyst particles are visible as the bright areas (region 1-2)). XPS spectra of (d) O 1s, (g) Sr 3d, (h) Co 2p, and (i) Ni 2p in pristine and post-mortem PTLs after 20 h stability test at 0.5 A cm^{-2} with pure water feed in AEMWEs for $Sr_{0.1}La_{0.9}Co_{0.5}Ni_{0.5}O_3$ sample.

XRD measurements of $Sr_{0.1}La_{0.9}Co_{0.5}Ni_{0.5}O_3$ were also carried out before and after the stability test (**Figure 3a**). The post-test XRD data revealed no additional peaks, indicating that the bulk crystalline structure remained intact, although this data does not preclude significant surface reconstructions. XPS collected for $Sr_{0.1}La_{0.9}Co_{0.5}Ni_{0.5}O_3$ showed the Sr 3d peak nearly vanished (from 2.25 atom % in the pristine sample to 0.14 atom % after 20-h operation at 0.5 A cm^{-2}), confirming Sr leaching (**Figure 3g**). To distinguish leaching from surface-masking effects, Sr signals were normalized against La, Co, and Ni. The Sr/La, Sr/Co, and Sr/Ni atomic ratios decreased from 0.30, 0.88, and 0.17 (pristine) to 0.17, 0.29, and 0.10 (post-test), respectively. While absolute XPS quantification can be confounded by surface adsorbates, this data across elemental references is strong evidence of Sr leaching during operation. In the O 1s spectra, the characteristic peak at ~528 eV associated with lattice oxygen lost intensity due to the formation of metal hydroxides on the perovskite surface (**Figure 3d**). Co 2p spectra changed less after the stability test, while the fitted intensity of a possible Ni^{2+} $2p_{3/2}$ peak in the Ni 2p spectra increased (**Figure 3h–i**). Co^{2+}/Ni^{2+} is originated from the existence of oxygen vacancies on the surface of perovskite oxides, which induces charge compensation by reducing adjacent Co^{3+}/Ni^{3+} ions to Co^{2+}/Ni^{2+}.[44,45] Together, these results indicate that $Sr_{0.1}La_{0.9}Co_{0.5}Ni_{0.5}O_3$ underwent surface reconstruction, probably yielding a Ni-rich Ni/Co (oxy)hydroxide on the surface that hosts the active catalyst after Sr leaching, while the core retained its crystalline perovskite structure that is electrically conductive.

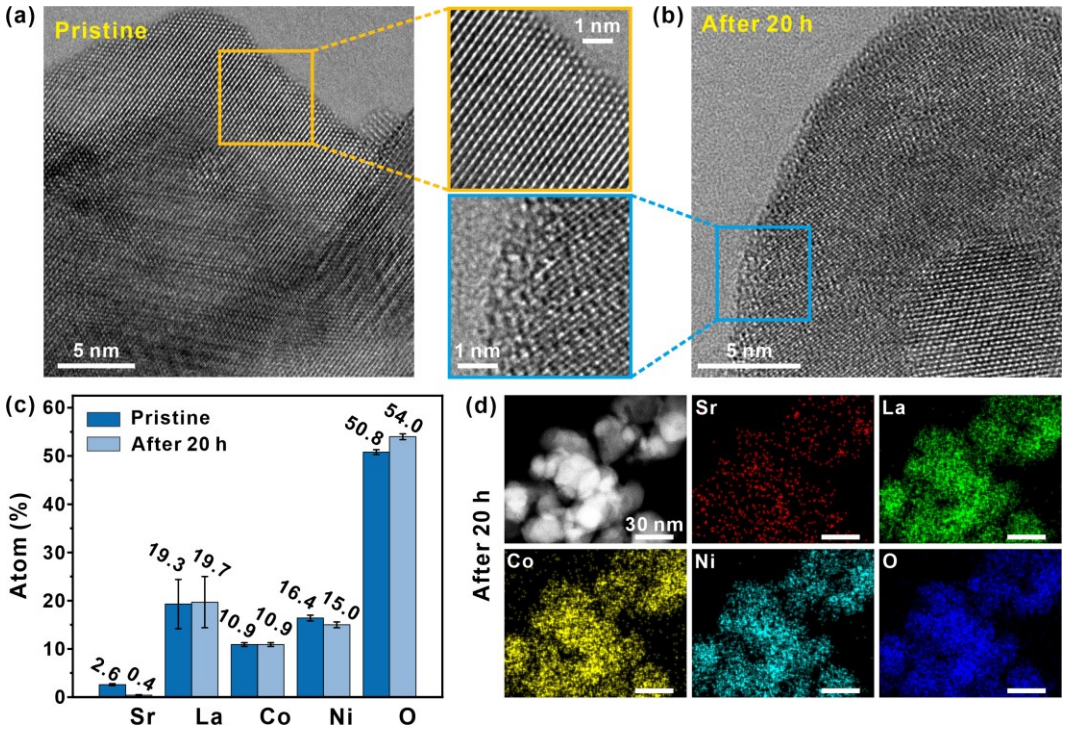

Figure 4. Structure and oxidation state of $Sr_{0.1}La_{0.9}Co_{0.5}Ni_{0.5}O_3$ on PTLs before and after operation. High-resolution transmission-electron-microscopy (HR-TEM) images of $Sr_{0.1}La_{0.9}Co_{0.5}Ni_{0.5}O_3$ (a) before and (b) after 20 h stability test at the current density of 500 mA cm^{-2}. (c) The average element distributions of $Sr_{0.1}La_{0.9}Co_{0.5}Ni_{0.5}O_3$ sample before and after AEMWE stability test from HAADF-STEM EDS element mapping. (d) HAADF-STEM image and corresponding EDS element mappings of $Sr_{0.1}La_{0.9}Co_{0.5}Ni_{0.5}O_3$ sample after AEMWE stability test.

For the $Sr_{0.1}La_{0.9}Co_{0.5}Ni_{0.5}O_3$ after 20-h operation in the AEMWE cell, TEM analysis showed only a thin disordered layer (~ 2 nm) on the surface, with the core crystalline structure retained (**Figure 4a–b**). The average compositions of the particles before and after testing were calculated from the entire image (**Figures 1f and 4c–d**). All the elements are similar, except for Sr, which changed from 2.6 ± 0.2 atom % to 0.4 ± 0.1 atom % after testing. This finding is consistent with XPS results; Sr leaches from $Sr_{0.1}La_{0.9}Co_{0.5}Ni_{0.5}O_3$ during the AEMWE operation. The reconstructed layer hypothesized from Sr-loss and XPS analysis was not visible in HR-TEM analysis. This result illustrates the difficulty in directly imaging electrochemically active disordered surface layers in these catalyst structures, despite their almost-certain presence based on the electrochemical and surface analyses.

Surface reconstruction of perovskite catalysts in Fe-free KOH electrolyte. To investigate the surface reconstruction of perovskite catalysts during water oxidation, cyclic voltammetry (CV) tests were conducted on the prepared perovskite catalysts with 10 wt%

PiperION ionomers on Pt/Ti quartz-crystal electrodes in 1.0 M rigorously Fe-free KOH electrolyte[46] using a standard three-electrode cell. This setup aims to simplify the analysis compared to the complexity of AEMWE system, although due to the use of liquid versus solid-ionomer electrolytes. The current densities were normalized by the BET specific surface areas to evaluate the intrinsic OER activities.

$Sr_{0.1}La_{0.9}Ni_{0.5}Co_{0.5}O_3$ exhibited the highest OER activity among all prepared perovskites whereas $LaNiO_3$ showed the worst performance, consistent with need for Fe-impurity activation for Ni-based OER catalysts (**Figure 5a**). The addition of Co at the Ni site in $LaNi_{0.5}Co_{0.5}O_3$ improved activity compared to $LaNiO_3$. For $Sr_{0.1}La_{0.9}Ni_{0.5}Co_{0.5}O_3$, the emergence of a redox wave at ~ 1.34 V vs. RHE in the pre-OER region is indicative of the generation of (oxy)hydroxide species induced by the surface reconstruction (inset of **Figure 5b**). This redox peak increased in intensity with cycling, becoming prominent after 25 cycles. Ni-containing perovskite catalysts developed redox peaks at ~1.43 V vs. RHE for $LaNiO_3$ and ~1.39 V vs. RHE for $LaCo_{0.5}Ni_{0.5}O_3$ (inset of **Figure 5c**). In contrast, $LaCoO_3$ did not exhibit observable redox peaks even after extended cycling, consistent with previous results that $LaNiO_3$ is prone to surface reconstruction while $LaCoO_3$ maintains greater structural stability.[25] The observed redox reaction preceding the OER for $LaNiO_3$-based perovskites corresponds to the reversible transition of $Ni(OH)_2$ to NiOOH.

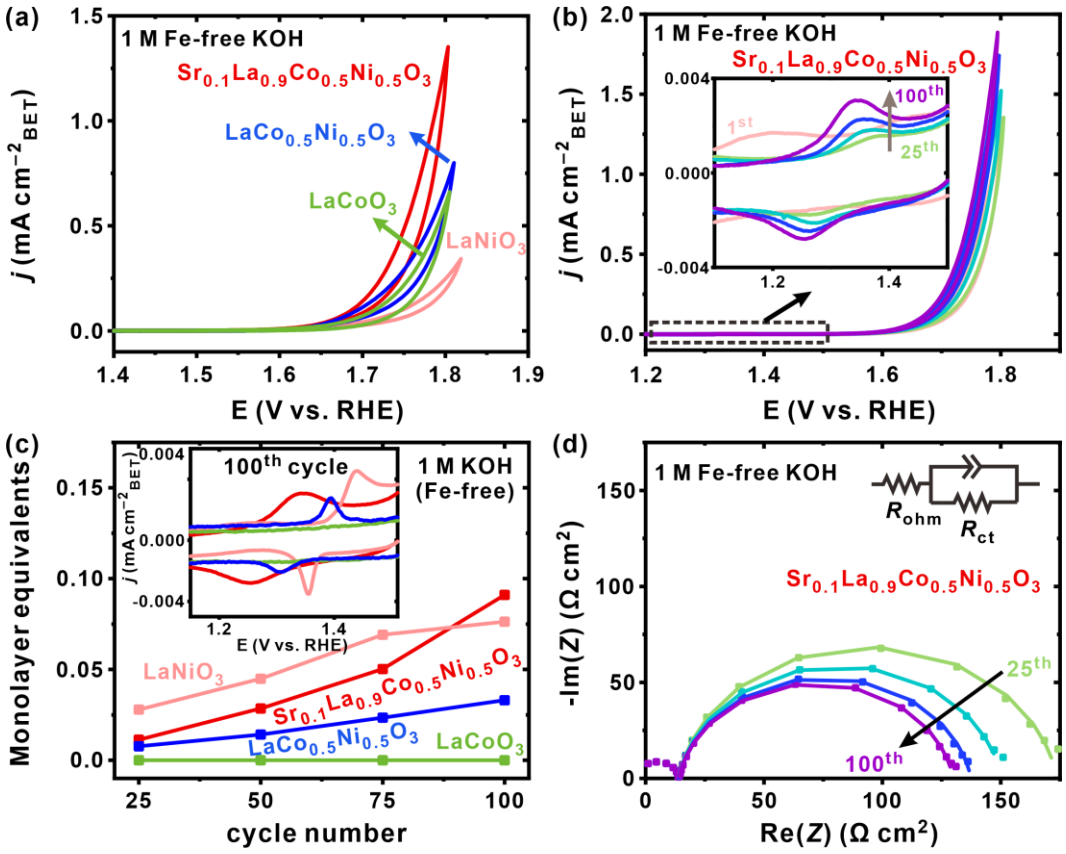

Figure 5. Three-electrode electrochemical studies as-prepared perovskite catalysts in 1.0 M Fe-free KOH solution. (a) CV tests at a scan rate of 10 mV s^{-1} for catalysts with 10 wt% PiperION on Pt/Ti quartz-crystal-microbalance electrodes (mass loading: 10 ± 1 μg cm^{-2}) tested in 1.0 M Fe-free KOH electrolyte. The current density is calculated using the BET surface areas of the catalyst powders. The overpotential was *iR* corrected (R_u: 3 ± 0.5 Ω cm^2). (b) CV cycling of $Sr_{0.1}La_{0.9}Co_{0.5}Ni_{0.5}O_3$ in 1.0 M Fe-free KOH electrolyte. Inset: the magnified redox peaks of $Sr_{0.1}La_{0.9}Co_{0.5}Ni_{0.5}O_3$ after 1, 25, 50, 75 and 100 cycles in the pre-OER region. (c) The number of nominal $Ni(OH)_2$ monolayer equivalents (MLE) obtained from the integrated charge of the redox peaks in the non-OER region of CV curve of perovskite samples. Inset: the magnified redox peaks of as-prepared perovskites after 100 cycles preceding to OER region. (d) EIS of $Sr_{0.1}La_{0.9}Co_{0.5}Ni_{0.5}O_3$ at 1.7 V vs. RHE after 25, 50, 75, 100 CV cycles in 1.0 M Fe-free KOH electrolyte. Inset: the equivalent circuit used to fit the data.

The number of redox-active $Ni(OH)_2$ can be estimated by integrating the Ni oxidation peak,[21,47] with the monolayer equivalents (MLE) of the reconstructed nickel hydroxide layer calculated using an average of 1.7 nmol Ni cm^{-2} per MLE (verified using the lattice parameters of β-$Ni(OH)_2$: a = b = 3.126 Å and 1 Ni atom per unit cell).[21,25] The MLE values of $Ni(OH)_2$ generated after 100 cycles on the surface of $LaNiO_3$, $LaCo_{0.5}Ni_{0.5}O_3$ and $Sr_{0.1}La_{0.9}Co_{0.5}Ni_{0.5}O_3$ were 0.08, 0.03 and 0.09, respectively (**Figure 5c**). The lower MLE growth rate for $LaCo_{0.5}Ni_{0.5}O_3$, compared to $LaNiO_3$, is attributed to the introduction of

more-stable Co-O bonds and active sites. $Sr_{0.1}La_{0.9}Co_{0.5}Ni_{0.5}O_3$ had a higher growth rate of redox-active oxyhydroxide than $LaCo_{0.5}Ni_{0.5}O_3$ likely due to Sr leaching during OER that facilitated the reconstruction of amorphous layer.[48] Regardless, all the perovskites yielded a thin layer of redox-active Ni species on the surface while preserving the core perovskite structure, which we hypothesize is important for high performance in the liquid-electrolyte-free AEMWE cells. The post-mortem HR-TEM images on the catalyst powders removed from EQCM electrodes after 100 cycles of CV cycling in 1 M Fe-free KOH and chronopotentiometric (CP) testing in 0.1 M Fe-free KOH (**Figure S27**) also demonstrated putative surface reconstruction under the supporting electrolyte environment, akin to observations in pure-water conditions (**Figure S28**). To investigate the influence of the generated redox-active metal (oxy)hydroxide species on charge transfer resistance (R_{ct}), PEIS of $Sr_{0.1}La_{0.9}Co_{0.5}Ni_{0.5}O_3$ was analyzed every 25 cycles at 1.7 V vs. RHE in the three-electrode 1.0 M Fe-free KOH cell (**Figure 5d**). The R_{ct} values decreased with the increased cycles attributed to the higher intrinsic activity of the reconstructed redox-active Ni species, consistent with the observed increased activity after cycling (**Figure 5b**).

CONCLUSIONS

We reported how to co-design mixed metal perovskite oxides for high electrical conductivity (metallic behaviour) along with surfaces that optimally reconstruct in a controlled way to form highly active sites for water oxidation catalysis. Starting with the parent $LaNiO_3$, the substitution of Co on the Ni sites marginally reduces electrical conductivity, but provides higher catalytic activity for the oxygen-evolution in pure-water alkaline ionomer conditions (and without the need for Fe impurities that activate catalysts in KOH tests).[25] The substitution of Sr on La sites both increases the degree of surface reconstruction due to the higher solubility of Sr^{2+} and decreases the nanoparticle size to increase the effective surface area. The best $Sr_{0.1}La_{0.9}Co_{0.5}Ni_{0.5}O_3$ catalyst provides exceptional activity in pure-water-fed AEMWE test platforms, with a total cell voltage of 1.97 ± 0.02 V at 2.0 A cm^{-2}; at least 200 mV lower than the IrO_2 baseline (at the same mass loading of 3.0 mg cm^{-2}) and better than reported pure-water electrolyzer devices.[15,18]

The advanced cell performance is the result of solid-state chemical design of catalyst in the anode resulting in high electrical conductivity that leads to large effective surface areas in the porous anode for water oxidation, while controlled surface reconstruction by tuned 10% Sr incorporation and leaching facilitates formation of the optimal thickness of the surface-active phase. Optimized Co substitution stabilizes the bulk lattice, confining reconstruction to a self-limiting ~2 nm amorphous surface layer and retaining metallic conductivity. The same high electrical conductivity and porous electrode architecture, however, also accelerates ionomer degradation at the catalyst/ionomer interface, known to be the durability limiting process in AEMWEs. This challenge remains to be fully solved, for example by interface engineering and passivation.[39] This work thus provides key insight for solid state chemical design of conductive perovskite anode catalysts in pure-water-fed AEMWEs thus contributing both to the science of electrocatalysis and practical goals of enabling efficient and cost-effective alkaline membrane electrolysis systems.

ASSOCIATED CONTENT

Supporting Information

The Supporting Information is available free of charge at http://pubs.acs.org.

Methods for preparation and characterization of perovskite catalysts; methods for electrode and MEA assembly preparation; electrochemical measurement methods for AEMWE operation and three-electrode cell tests; powder XRD patterns; SEM images along with corresponding particle size distribution analysis; polarization curves in AEMWE single-cell configuration; double-layer capacitance (C_{dl}) measurements; durability tests; surface SEM images with EDS elemental mapping and cross-sectional SEM images, HR-TEM images, and characterization data from XPS, ^{1}H-NMR spectra, ATR-FTIR spectra, XRD refinement, BET and ICP-MS measurements.

AUTHOR INFORMATION

Corresponding Authors

Zhengxiao Guo: zxguo@hku.hk; Shannon W. Boettcher: boettcher@berkeley.edu

Author contributions

The manuscript was written through contributions of all authors. All authors have given approval to the final version of the manuscript. [‡]T. Zhai and H. Wang contributed equally.

Notes

The authors declare the following competing financial interest(s): The authors have filed a provisional patent application on materials reported in this manuscript and are working to commercialize advanced catalyst compositions for AEMWEs.

ACKNOWLEDGMENTS

The development of the perovskite catalyst composition and materials characterization work was supported by the National Science Foundation Chemical Catalysis Program Award #2400195. The analysis of the perovskite oxide catalysts in alkaline membrane electrolyzers was supported by the U.S. Department of Energy under award DE-EE0011322 and initial device testing was supported under award DE-EE0008841. T. Z. acknowledges support from the UGC-TRS award (T23-713/22-R), the RGC-GRF award (17300424) and National Natural Science Foundation of China (22305225). We acknowledge the use of shared instrumentation in the Center for Advanced Materials Characterization in Oregon (CAMCOR). Lihaokun Chen is thanked for assistance with electrolyzer cell design and measurements. Yang Zhao is thanked for manuscript revision.

REFERENCES

(1) Abbasi, R.; Setzler, B. P.; Lin, S.; Wang, J.; Zhao, Y.; Xu, H.; Pivovar, B.; Tian, B.; Chen, X.; Wu, G. A roadmap to low-cost hydrogen with hydroxide exchange membrane electrolyzers. *Adv. Mater.* **2019**, *31* (31), No. 1805876.

(2) Jin, H.; Ruqia, B.; Park, Y.; Kim, H. J.; Oh, H. S.; Choi, S. I.; Lee, K. Nanocatalyst design for long-term operation of proton/anion exchange membrane water electrolysis. *Adv. Energy Mater.* **2021**, *11* (4), No. 2003188.

(3) Yan, Z.; Hitt, J. L.; Turner, J. A.; Mallouk, T. E. Renewable electricity storage using electrolysis. *Proc. Natl. Acad. Sci.* **2020**, *117* (23), 12558–12563.

(4) Mefford, J. T.; Akbashev, A. R.; Kang, M.; Bentley, C. L.; Gent, W. E.; Deng, H. D.; Alsem, D. H.; Yu, Y.-S.; Salmon, N. J.; Shapiro, D. A. Correlative operando microscopy of oxygen evolution electrocatalysts. *Nature* **2021**, *593* (7857), 67–73.

(5) Wang, H.; Zhai, T.; Wu, Y.; Zhou, T.; Zhou, B.; Shang, C.; Guo, Z. High-valence oxides for high performance oxygen evolution electrocatalysis. *Adv. Sci.* **2023**, *10* (22), No. 2301706.

(6) Henkensmeier, D.; Cho, W.-C.; Jannasch, P.; Stojadinovic, J.; Li, Q.; Aili, D.; Jensen, J. O. Separators and membranes for advanced alkaline water electrolysis. *Che. Rev.* **2024**, *124* (10), 6393–6443.

(7) Ayers, K.; Danilovic, N.; Ouimet, R.; Carmo, M.; Pivovar, B.; Bornstein, M. Perspectives on low-temperature electrolysis and potential for renewable hydrogen at scale. *Annu. Rev. Chem. Biomol. Eng.* **2019**, *10*, 219–239.

(8) Liu, R.-T.; Xu, Z.-L.; Li, F.-M.; Chen, F.-Y.; Yu, J.-Y.; Yan, Y.; Chen, Y.; Xia, B. Y. Recent advances in proton exchange membrane water electrolysis. *Chem. Soc. Rev.* **2023**, *52*, 5652–5683.

(9) Chen, Z.; Guo, L.; Pan, L.; Yan, T.; He, Z.; Li, Y.; Shi, C.; Huang, Z. F.; Zhang, X.; Zou, J. J. Advances in oxygen evolution electrocatalysts for proton exchange membrane water electrolyzers. *Adv. Energy Mater.* **2022**, *12* (14), No. 2103670.

(10) Du, N.; Roy, C.; Peach, R.; Turnbull, M.; Thiele, S.; Bock, C. Anion-exchange membrane water electrolyzers. *Chem. Rev.* **2022**, *122* (13), 11830–11895.

(11) Chen, P.; Hu, X. High-efficiency anion exchange membrane water electrolysis employing non-noble metal catalysts. *Adv. Energy Mater.* **2020**, *10* (39), No. 2002285.

(12) Razmjooei, F.; Morawietz, T.; Taghizadeh, E.; Hadjixenophontos, E.; Mues, L.; Gerle, M.; Wood, B. D.; Harms, C.; Gago, A. S.; Ansar, S. A. Increasing the performance of an anion-exchange membrane electrolyzer operating in pure water with a nickel-based microporous layer. *Joule* **2021**, *5* (7), 1776–1799.

(13) Becker, H.; Murawski, J.; Shinde, D. V.; Stephens, I. E.; Hinds, G.; Smith, G. Impact of impurities on water electrolysis: a review. *Sustain. Energy Fuels* **2023**, *7* (7), 1565–1603.

(14) Wu, L.; Ning, M.; Xing, X.; Wang, Y.; Zhang, F.; Gao, G.; Song, S.; Wang, D.; Yuan, C.; Yu, L. Boosting oxygen evolution reaction of (Fe, Ni)OOH via defect engineering for anion exchange membrane water electrolysis under industrial conditions. *Adv. Mater.* **2023**, *35* (44), No. 2306097.

(15) Shaik, S.; Kundu, J.; Yuan, Y.; Chung, W.; Han, D.; Lee, U.; Huang, H.; Choi, S. I. Recent progress and perspective in pure water-fed anion exchange membrane water electrolyzers. *Adv. Energy Mater.* **2024**, No. 2401956.

(16) Li, D.; Park, E. J.; Zhu, W.; Shi, Q.; Zhou, Y.; Tian, H.; Lin, Y.; Serov, A.; Zulevi, B.; Baca, E. D. Highly quaternized polystyrene ionomers for high performance anion exchange membrane water electrolysers. *Nat. Energy* **2020**, *5* (5), 378–385.

(17) Krivina, R. A.; Ou, Y.; Xu, Q.; Twight, L. P.; Stovall, T. N.; Boettcher, S. W. Oxygen

electrocatalysis on mixed-metal oxides/oxyhydroxides: from fundamentals to membrane electrolyzer technology. *Acc. Mater. Res.* **2021**, *2* (7), 548–558.

(18) Krivina, R. A.; Lindquist, G. A.; Beaudoin, S. R.; Stovall, T. N.; Thompson, W. L.; Twight, L. P.; Marsh, D.; Grzyb, J.; Fabrizio, K.; Hutchison, J. E. Anode catalysts in anion-exchange-membrane electrolysis without supporting electrolyte: conductivity, dynamics, and ionomer degradation. *Adv. Mater.* **2022**, *34* (35), No. 2203033.

(19) Ngo, Q. P.; Nguyen, T. T.; Le, Q. T. T.; Lee, J. H.; Kim, N. H. Unveiling the synergistic effect of atomic iridium modulated zirconium-doped pure phase cobalt phosphide for robust anion-exchange membrane water electrolyzer. *Adv. Energy Mater.* **2023**, *13* (44), No. 2301841.

(20) Xu, D.; Stevens, M. B.; Cosby, M. R.; Oener, S. Z.; Smith, A. M.; Enman, L. J.; Ayers, K. E.; Capuano, C. B.; Renner, J. N.; Danilovic, N. Earth-abundant oxygen electrocatalysts for alkaline anion-exchange-membrane water electrolysis: effects of catalyst conductivity and comparison with performance in three-electrode cells. *ACS Catal.* **2018**, *9* (1), 7–15.

(21) Batchellor, A. S.; Boettcher, S. W. Pulse-electrodeposited Ni–Fe (oxy) hydroxide oxygen evolution electrocatalysts with high geometric and intrinsic activities at large mass loadings. *ACS Catal.* **2015**, *5* (11), 6680–6689.

(22) Cao, C.; Shang, C.; Li, X.; Wang, Y.; Liu, C.; Wang, X.; Zhou, S.; Zeng, J. Dimensionality control of electrocatalytic activity in perovskite nickelates. *Nano Lett.* **2020**, *20* (4), 2837–2842.

(23) Son, J.; LeBeau, J. M.; Allen, S. J.; Stemmer, S. Conductivity enhancement of ultrathin $LaNiO_3$ films in superlattices. *Appl. Phys. Lett.* **2010**, *97* (20), No. 202109.

(24) Fowlie, J.; Gibert, M.; Tieri, G.; Gloter, A.; Íñiguez, J.; Filippetti, A.; Catalano, S.; Gariglio, S.; Schober, A.; Guennou, M. Conductivity and local structure of $LaNiO_3$ thin films. *Adv. Mater.* **2017**, *29* (18), No. 1605197.

(25) Twight, L.; Tonsberg, A.; Samira, S.; Velinkar, K.; Dumpert, K.; Ou, Y.; Wang, L.; Nikolla, E.; Boettcher, S. W. Trace Fe activates perovskite nickelate OER catalysts in alkaline media via redox-active surface Ni species formed during electrocatalysis. *J. Catal.* **2024**, *432*, No. 115443.

(26) Kong, T.-H.; Thangavel, P.; Shin, S.; Kwon, S.; Choi, H.; Lee, H.; Park, N.; Woo, J.-J.; Kwon, Y. *In-situ* ionomer-free catalyst-coated membranes for anion exchange membrane water electrolyzers. *ACS Energy Lett.* **2023**, *8* (11), 4666–4673.

(27) Tricker, A. W.; Ertugrul, T. Y.; Lee, J. K.; Shin, J. R.; Choi, W.; Kushner, D. I.; Wang, G.; Lang, J.; Zenyuk, I. V.; Weber, A. Z. Pathways toward efficient and durable anion exchange membrane water electrolyzers enabled by electro-Active porous transport layers. *Adv. Energy Mater.* **2024**, *14* (9), No. 2303629.

(28) Karmakar, A.; Senthamaraikannan, T. G.; Baasanjav, E.; Bandyopadhyay, P.; Jin, B.; Park, Y. S.; Lim, D.-H.; Jeong, S. M. Surface hydroxyl group-enriched nickel cobalt molybdate hydrate for improved oxygen evolution activity in an anion exchange membrane water electrolyzer. *Appl. Catal. B: Environ.* **2023**, *328*, No. 122504.

(29) Shi, Z.; Li, J.; Wang, Y.; Liu, S.; Zhu, J.; Yang, J.; Wang, X.; Ni, J.; Jiang, Z.; Zhang, L. Customized reaction route for ruthenium oxide towards stabilized water oxidation in high-performance PEM electrolyzers. *Nat. Commun.* **2023**, *14* (1), No. 843.

(30) Liu, H.; Zhang, Z.; Fang, J.; Li, M.; Sendeku, M. G.; Wang, X.; Wu, H.; Li, Y.; Ge, J.; Zhuang, Z. Eliminating over-oxidation of ruthenium oxides by niobium for highly stable electrocatalytic oxygen evolution in acidic media. *Joule* **2023**, *7* (3), 558–573.

(31) Wang, Y.; Zhang, M.; Kang, Z.; Shi, L.; Shen, Y.; Tian, B.; Zou, Y.; Chen, H.; Zou, X. Nano-metal diborides-supported anode catalyst with strongly coupled TaO_x/IrO_2 catalytic layer for low-iridium-loading proton exchange membrane electrolyzer. *Nat. Commun.* **2023**, *14* (1), No. 5119.

(32) Liu, J.; Jia, E.; Wang, L.; Stoerzinger, K. A.; Zhou, H.; Tang, C. S.; Yin, X.; He, X.; Bousquet,

E.; Bowden, M. E. Tuning the electronic structure of $LaNiO_3$ through alloying with strontium to enhance oxygen evolution activity. *Adv. Sci.* **2019**, *6* (19), No. 1901073.

(33) Lee, J.; Jung, H.; Park, Y. S.; Woo, S.; Yang, J.; Jang, M. J.; Jeong, J.; Kwon, N.; Lim, B.; Han, J. W. High-efficiency anion-exchange membrane water electrolyzer enabled by ternary layered double hydroxide anode. *Small* **2021**, *17* (28), No. 2100639.

(34) Liu, J.; Kang, Z.; Li, D.; Pak, M.; Alia, S. M.; Fujimoto, C.; Bender, G.; Kim, Y. S.; Weber, A. Z. Elucidating the role of hydroxide electrolyte on anion-exchange-membrane water electrolyzer performance. *J. Electrochem. Soc.* **2021**, *168* (5), No. 054522.

(35) Qi, Y.; Liu, J.; Sabarirajan, D. C.; Huang, Y.; Perego, A.; Haug, A. T.; Zenyuk, I. V. Interpreting ionic conductivity for polymer electrolyte fuel cell catalyst layers with electrochemical impedance spectroscopy and transmission line modeling. *J. Electrochem. Soc.* **2021**, *168* (5), No. 054502.

(36) Thangavel, P.; Ha, M.; Kumaraguru, S.; Meena, A.; Singh, A. N.; Harzandi, A. M.; Kim, K. S. Graphene-nanoplatelets-supported NiFe-MOF: high-efficiency and ultra-stable oxygen electrodes for sustained alkaline anion exchange membrane water electrolysis. *Energy Environ. Sci.* **2020**, *13* (10), 3447–3458.

(37) Li, D.; Matanovic, I.; Lee, A. S.; Park, E. J.; Fujimoto, C.; Chung, H. T.; Kim, Y. S. Phenyl oxidation impacts the durability of alkaline membrane water electrolyzer. *ACS Appl. Mater. Interfaces.* **2019**, *11* (10), 9696–9701.

(38) Lindquist, G. A.; Gaitor, J. C.; Thompson, W. L.; Brogden, V.; Noonan, K. J.; Boettcher, S. W. Oxidative instability of ionomers in hydroxide-exchange-membrane water electrolyzers. *Energy Environ. Sci.* **2023**, *16* (10), 4373–4387.

(39) Kwak, M.; Ojha, K.; Shen, M.; Boettcher, S. W. Electrically insulated catalyst–ionomer anode interfaces toward durable alkaline membrane electrolyzers. *ACS Energy Lett.* **2024**, *9*, 1025–1034.

(40) Dang, H.-S.; Jannasch, P. A. comparative study of anion-exchange membranes tethered with different hetero-cycloaliphatic quaternary ammonium hydroxides. *J. Mater. Chem. A* **2017**, *5* (41), 21965–21978.

(41) Yuan, W.; Zeng, L.; Jiang, S.; Yuan, C.; He, Q.; Wang, J.; Liao, Q.; Wei, Z. High performance poly (carbazolyl aryl piperidinium) anion exchange membranes for alkaline fuel cells. *J. Membr. Sci.* **2022**, *657*, No. 120676.

(42) Krivina, R. A.; Lindquist, G. A.; Yang, M. C.; Cook, A. K.; Hendon, C. H.; Motz, A. R.; Capuano, C.; Ayers, K. E.; Hutchison, J. E.; Boettcher, S. W. Three-electrode study of electrochemical ionomer degradation relevant to anion-exchange-membrane water electrolyzers. *ACS Appl. Mater. Interfaces* **2022**, *14* (16), 18261–18274.

(43) Park, J.-H.; Park, Y.; Jeon, T.-S.; Seo, Y.; Park, J.-S. Impact of cross-linking-monomer characteristics on pore-filling-membrane performance and durability in anion-exchange water electrolysis. *Appl. Sci.* **2025**, *15* (3), No. 1495.

(44) Kim, N. I.; Lee, J.; Jin, S.; Park, J.; Jeong, J. Y.; Lee, J.; Kim, Y.; Kim, C.; Choi, S. M. Synergistic effects in $LaNiO_3$ perovskites between nickel and iron heterostructures for improving durability in oxygen evolution reaction for AEMWE. *Small Methods* **2024**, *8* (9), No. 2400284.

(45) Shi, Z.; Dong, F.; Tang, Z.; Dong, X. Design Sr, Mn-doped 3DOM $LaCoO_3$ perovskite catalysts with excellent SO_2 resistance for benzene catalytic combustion. *Chem. Eng. J.* **2023**, *473*, No. 145476.

(46) Liu, L.; Twight, L. P.; Fehrs, J. L.; Ou, Y.; Sun, D.; Boettcher, S. W. Purification of residual Ni and Co hydroxides from Fe-free alkaline electrolyte for electrocatalysis studies. *ChemElectroChem* **2022**, *9* (15), No. e202200279.

(47) Stevens, M. B.; Enman, L. J.; Batchellor, A. S.; Cosby, M. R.; Vise, A. E.; Trang, C. D.; Boettcher, S. W. Measurement techniques for the study of thin film heterogeneous water oxidation electrocatalysts. *Chem. Mater.* **2017**, *29* (1), 120–140.

(48) Fabbri, E.; Nachtegaal, M.; Binninger, T.; Cheng, X.; Kim, B.-J.; Durst, J.; Bozza, F.; Graule, T.; Schäublin, R.; Wiles, L. Dynamic surface self-reconstruction is the key of highly active perovskite nano-electrocatalysts for water splitting. *Nat. Mater.* **2017**, *16* (9), 925–931.
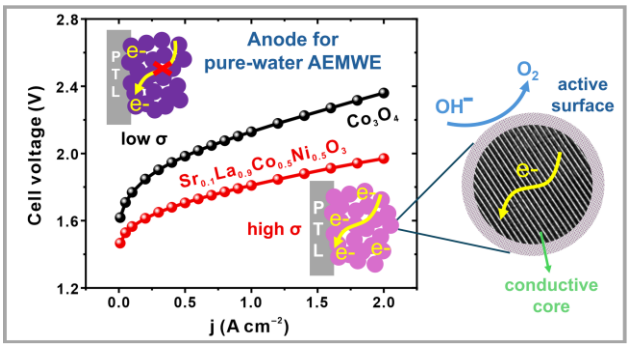
Table of Contents